Desalination and Water Treatment
www.deswater.com
doi: 10.5004/dwt.2021.27267

226 (2021) 419–430
June

Sulfhydryl modified β-cyclodextrin/Fe_3O_4/graphene oxide magnetic nanohybrid for the adsorption of silver ions and cationic dye methylene blue

Xin Li, Yingxia Ma*, Xiaofeng Shi, Xiaoya Kang, Fengming Bai, Dingjun Zhang

State Key Laboratory of Advanced Processing and Recycling of Nonferrous Metals, School of Materials Science and Engineering, Lanzhou University of Technology, Lanzhou 730050, China, Tel. +86-15193189130/+86-15119319130; email: mayx2011818@163.com (Y. Ma), Tel. +86-13993156361; email: lix941021@163.com (X. Li), Tel. +86-18894576792; email: shixf0629@163.com (X. Shi), Tel. +86-15293182053; email: 15293182053@163.com (X. Kang), Tel. +86-17339881973; email: bfm1995@163.com (F. Bai), Tel. +86-13609321215; email: zhangdingjunlut@163.com (D. Zhang)

Received 10 December 2020; Accepted 21 March 2021

ABSTRACT

Sulfhydryl modified β-cyclodextrin/Fe_3O_4/graphene oxide magnetic nanohybrid (β-CD/Fe_3O_4/GO-SH) was prepared using 3-mercaptopropyltrimethoxysilane functionalized β-cyclodextrin/Fe_3O_4/graphene oxide magnetic nanohybrid (β-CD/Fe_3O_4/GO) fabricated by a one-step reverse-phase co-precipitation method. The obtained β-CD/Fe_3O_4/GO-SH sample was characterized by transmission electron microscope, X-ray diffraction, Fourier-transform infrared spectroscopy, N_2 adsorption/desorption isotherm, X-ray photoelectron spectroscopy (XPS), thermogravimetric analysis and vibrating sample magnetometer. The adsorption property of β-CD/Fe_3O_4/GO-SH for silver ions (Ag(I)) and cationic dye methylene blue (MB) in a single system was investigated by batch experiments. The results indicated that the β-CD/Fe_3O_4/GO-SH as superparamagnetic adsorption material with magnetic separation property in aqueous solution was successfully prepared. The maximum adsorption capacity of the β-CD/Fe_3O_4/GO-SH for Ag(I) and MB was 101.87 and 105.74 mg g^{-1}, respectively. The XPS analysis results affirmed that the sulfhydryl groups of the β-CD/Fe_3O_4/GO-SH displayed a superior affinity for Ag(I), and Ag(I) was reduced to Ag element during the adsorption process. The adsorption process of the β-CD/Fe_3O_4/GO-SH for Ag(I) and MB conformed to the pseudo-second-order kinetic model representing the adsorption process as predominantly chemisorption. The adsorption equilibrium data of the β-CD/Fe_3O_4/GO-SH for Ag(I) and MB had better agreement with the Freundlich isothermal model and the Langmuir model, respectively, indicating that the isothermal adsorption process of the β-CD/Fe_3O_4/GO-SH for Ag(I) and MB was heterogeneous multilayer adsorption and homogeneous monolayer adsorption, respectively.

Keywords: β-cyclodextrin/Fe_3O_4/graphene oxide; Sulfhydryl; Adsorption; Silver ions; Methylene blue

1. Introduction

With the development of modern industries and the progress of human society, water resources around the world have heavily contaminated by heavy metal ions and dye molecules, posing a great threat to human health and ecological balance. Among many heavy metal ions pollution, silver ion (Ag(I)) contamination mainly derives from industrial wastewater discharged from photography, electroplating, catalysis, batteries, medical equipment, and other fields. Accompanied by the water circulation system, Ag(I) is intermingled with groundwater or exposed to the air

* Corresponding author.

and then accumulates in human bodies or animal somatic, which could gravely endanger human health and ecosystems [1,2]. Methylene blue (MB), as a typical cationic organic dye, is frequently applied as a major industrial raw material in many fields, such as textiles, cosmetics, printing and dyeing, food processing, and paper manufacturing [3]. One of the synthetic dyes MB is toxic in nature, and can cause permanent damage to the skin and eyes as well as nausea, vomiting, diarrhea, sweating and other symptoms [4,5].

Given the current status, hazards of the pollution caused by dyes and heavy metal ions, the removal of dyes and heavy metal ions from wastewater is of utmost importance to ensure human health and environmental safety. There are various wastewater treatment technologies for the removal of dyes or heavy metal ions, such as chemical precipitation, ion exchange, adsorption, membrane filtration, and electrochemistry [6], among which the adsorption process is deemed an optimal choice due to its simple design, easy handling, wide adaptability, high efficiency and economic viability [7]. Activated carbon [8], bottom ash [9], clay, metal-organic framework [10], and natural biosorbents [7,11] have been implemented for the removal of dye molecules or heavy metal ions as adsorbent materials. Nevertheless, cyclodextrin-based adsorbents have been valued in this field for their distinctive structural properties [12–15]. β-cyclodextrin is a non-toxic, biodegradable cyclic oligosaccharide obtained by starch biodegradation, consists of α-1,4-glucoside linked to seven D-glucose units, and has the structural property of "hydrophobic inner cavity and hydrophilic outer wall" [16]. The peculiar structure and properties allow β-cyclodextrin as a host to selectively enclose diverse guest molecules such as dyes and heavy metal ions [17]. And the hydroxyl groups on the outside of β-CD enable the binding of dyes and heavy metal ions via hydrogen bonding or electronic interactions and chelation [18], offering considerable potential for adsorption of pollutants in the aqueous system. However, the recycling of β-CD and its derivatives in the adsorption process was cumbersome and complicated for large-scale practical application.

To address this issue, graphene oxide (GO) with a large specific surface area as an excellent carrier loading magnetic Fe_3O_4 magnetic nanoparticles and grafting β-CD nanocomposites have been come into focus in recent years [19–21]. Furthermore, GO has a strong affinity for aromatic compounds and heavy metal ions due to the existence of delocalized π-electrons system and oxygen-containing functional groups [22].

To simplify the tedious preparation procedures and reduce the unnecessary costs, we first fabricated β-cyclodextrin/Fe_3O_4/graphene oxide (β-CD/Fe_3O_4/GO) magnetic nanohybrid by a simple one-step reverse-phase co-precipitation method in our previous work [23]. Considering the S atom in the sulfhydryl group appeared with a good affinity for Ag(I) [24] according to the soft and hard acid-base theory, and the $–S^-$ produced by the ionization of the sulfhydryl group could form complexes with the cation MB via electrostatic interactions. In this work, the β-CD/Fe_3O_4/GO magnetic nanohybrid was functionalized using 3-mercaptopropyltrimethoxysilane (3-MPTS) to prepare sulfhydryl modified β-CD/Fe_3O_4/GO (β-CD/Fe_3O_4/GO-SH) magnetic nanohybrid for adsorption of Ag(I) and cationic dye MB.

2. Experimental

2.1. Materials

Natural flake graphite (NFG) with a purity of 99 wt.% was supplied by Shandong Qingdao Tianhe Graphite Company (China) and passed through a 60 BS mesh sieve. GO was prepared from NFG by the modified Hummers method [25]. $FeCl_3·6H_2O$, β-CD and 3-MPTS were supplied by Shanghai Macklin Biochemical Co., Ltd., (China). $FeSO_4·7H_2O$, NaOH and methylbenzene were purchased from Tianjin Damao Chemical Co., Ltd., (China). MB and silver nitrate ($AgNO_3$) were obtained from Tianjin Kaitong Chemical Reagent Co., Ltd., (China). Anhydrous ethanol was derived from Tianjin Fuyu Chemical Co., Ltd., (China). All the chemicals were of analytical grade and used as received.

2.2. Synthesis of β-CD/Fe_3O_4/GO-SH

The β-CD/Fe_3O_4/GO was fabricated via the method in our previous report [23]. Briefly, dissolve 2.0 g of β-CD in 80 mL of deionized water containing 2.0 g of NaOH at 80°C. Subsequently, 50 mg of GO was evenly dispersed in 80 mL of deionized water containing 0.004 mol of $FeSO_4·7H_2O$ and 0.008 mol of $FeCl_3·6H_2O$ by sonication at room temperature, the above mixture from a constant pressure funnel was added dropwise to NaOH solution containing β-CD under mechanical stirring at the nitrogen atmosphere. The reaction was then continued by continuous stirring for 30 min, followed by lowering the reaction temperature to 50°C and continuing stirring for 1 h. The obtained black precipitates were collected by the magnet and washed sequentially with deionized water and anhydrous ethanol to remove the unreacted residual, followed by drying in vacuum at 50°C for 24 h to obtain the sample denoted as β-CD/Fe_3O_4/GO for use.

For the preparation of β-CD/Fe_3O_4/GO-SH, 50 mg of β-CD/Fe_3O_4/GO was uniformly dispersed into a 250 mL triple flask containing 80 mL of toluene, and then the system was heated to 110°C under low-speed mechanical agitation and N_2 protection, followed by the slow addition of 20 mL of 3-MPTS. After continuing the reaction for 48 h, the solid product was collected under an applied magnetic field, and rinsed thoroughly with anhydrous ethanol and deionized water, and then dried under vacuum at 50°C for 24 h, the obtained sample denoted as β-CD/Fe_3O_4/GO-SH.

2.3. Characterization

The sizes, morphologies and elemental composition of samples were investigated using a transmission electron microscope (TEM, JEM-2100F (JEOL, Japan)). Fourier-transform infrared spectroscopy (FTIR, Nexus 670 Thermo Electron Corporation, USA) was employed for the detection of chemical functional groups of samples. The X-ray diffraction (XRD) patterns of samples were recorded by an X-ray diffractometer (XRD, D/MAX-2400, Rigaku, Japan) with a Cu Ka radiation at the 2θ range of 5°–70°. N_2 adsorption/desorption isotherms, Brunauer–Emmett–Teller surface area and Barrett–Joyner–Halenda (BJH) pore size distribution measurements of the samples were performed by Micromeritics ASAP 2020 (USA). The thermal stability of samples was

obtained from thermogravimetric analysis (TGA, STA449C, Netzsch, Germany) under a nitrogen environment ranging from 25°C to 800°C. Measurement of magnetization of samples was conducted by a vibrating sample magnetometer (VSM, Lakeshore, America). X-ray photoelectron spectroscopy (XPS, Thermo Electron Corporation, USA) equipped with Al Kα monochromatic X-ray source was conducted to identify the surface elemental composition and the chemical valence. The zeta potential of the sample was tested by Malvern Zetasizer (British).

2.4. Adsorption experiments

$AgNO_3$ was used as the source of Ag(I). Batch adsorption experiments of the single-component system were performed that 50 mg adsorbent was dispersed into a 250 mL conical flask containing 50 mL MB or $AgNO_3$ aqueous solution, which fixed on a thermostatic oscillator to oscillate at 120 rpm for a certain time. The effect of pH value on adsorption properties was conducted by varying the pH value of MB or $AgNO_3$ aqueous solutions adjusted by NaOH and HNO_3 aqueous solution. At the end of the adsorption experiment, the solid adsorbent was separated under an applied magnetic field, and then the adsorption capacity was calculated from the difference between the initial and equilibrium concentrations of Ag(I) or MB, which was determined by UV-vis spectrophotometer. All adsorption experiments were performed in triplicate.

3. Results and discussion

3.1. Characterization of the samples

The surface morphology (a) and elemental composition (b) of β-CD/Fe_3O_4/GO-SH were analyzed by TEM images coupled with the corresponding selected area electron diffraction (SAED) patterns and energy-dispersive X-ray (EDX) spectra, as shown in Fig. 1. The noticeable several wrinkles (red arrow pointing) of the GO could be observed from Fig. 1a. Besides, numerous Fe_3O_4 nanoparticles with an average diameter of about 5 nm are uniformly anchored on the surface of GO. It is noteworthy that the distribution pattern and size of Fe_3O_4 nanoparticles presented in the TEM images of β-CD/Fe_3O_4/GO-SH are almost identical to those rendered by the β-CD/Fe_3O_4/GO in our group previous study [23]. As well, another interesting aspect is that the six diffraction rings of the crystalline faces of inverse spine-structured Fe_3O_4 are explicitly represented in the SAED patterns of β-CD/Fe_3O_4/GO from our previous report. However, for β-CD/Fe_3O_4/GO-SH, the SAED pattern (inset of Fig. 1a) only exhibits diffraction rings for (4 4 0) and (3 1 1) crystal faces appearing faint compared to the β-CD/Fe_3O_4/GO, which is caused by the introduction of amorphous 3-MPTS on the surface of β-CD/Fe_3O_4/GO. EDX spectra were implemented to analyze the elemental composition of the sample. The EDX spectra of β-CD/Fe_3O_4/GO-SH (Fig. 1b) contain the S and Si elements from 3-MPTS in addition to C, O, Cu, and Fe elements, thus validating the successful preparation of β-CD/Fe_3O_4/GO-SH. C and O elements are attributed to GO, β-CD and Fe_3O_4, while 3-MPTS also serves as the additional source of C and O elements. The existence of Fe_3O_4 of β-CD/Fe_3O_4/GO-SH is verified by the Fe peaks. Cu peaks originated from the copper grid for testing.

The XRD patterns of β-CD/Fe_3O_4/GO-SH before (a) and after adsorption Ag(I) (b) are displayed in Fig. 2. As seen in Fig. 2a, five conspicuous crystalline peaks yielded from (2 2 0), (3 1 1), (4 0 0), (5 1 1), and (4 4 0) planes of Fe_3O_4 occur at 30.4°, 35.4°, 43.1°, 56.9° and 62.6° [26], illustrating the possession of inverse spine-structured Fe_3O_4 nanoparticles in β-CD/Fe_3O_4/GO-SH. Moreover, the larger widths of the diffraction peaks of Fe_3O_4 are found to attest to the smaller Fe_3O_4 in size, which is consistent with the TEM characterization results. The crystalline peaks of Fe_3O_4 are also observed in the patterns of β-CD/Fe_3O_4/GO-SH after adsorption Ag(I) (Fig. 2b), along with five new diffraction peaks at 37.8°, 44.1°, 64.4°, 77.3° and 81.4° attributed to (1 1 1), (2 0 0), (2 2 0), (3 1 1) and (2 2 2) lattice planes from Ag nanoparticles with face-centered cubic structure, respectively, demonstrating that Ag(I) was successfully adsorbed by β-CD/Fe_3O_4/GO-SH and reduced to elemental Ag in the adsorption process.

To ascertain the successful modification of β-CD/Fe_3O_4/GO by sulfhydryl functional groups and the adsorption of MB on β-CD/Fe_3O_4/GO-SH, FTIR spectra analysis were carried on and are shown in Fig. 3. The absorption peak at

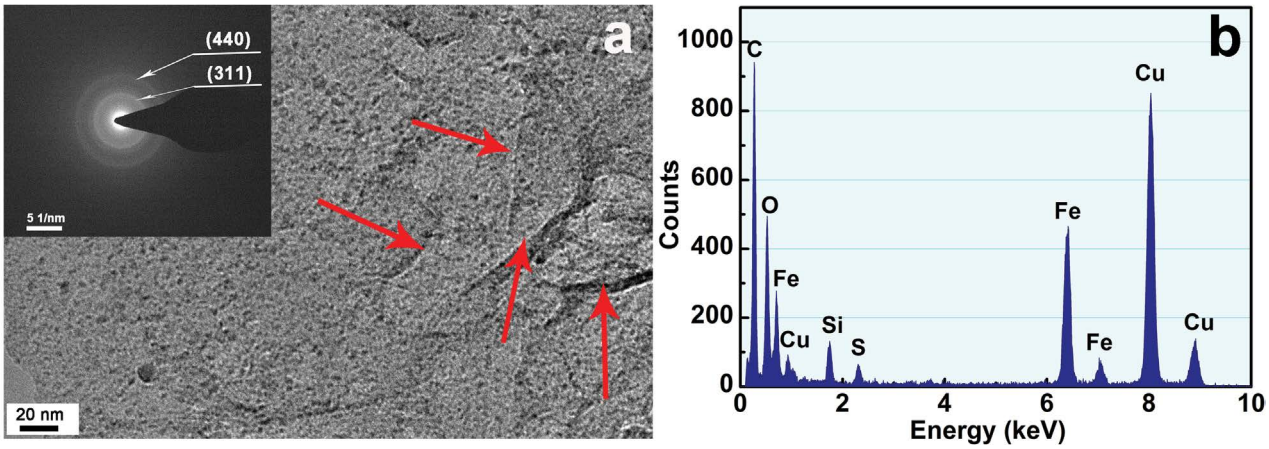

Fig. 1. TEM images (a), SAED pattern (inset) and EDX spectra (b) of β-CD/Fe_3O_4/GO-SH.

587 cm^{-1} in the spectra of β-CD/Fe_3O_4/GO-SH (Fig. 3a) is attributed to the Fe–O bond vibration [27], indicating the presence of Fe_3O_4 nanoparticles. The C=C stretching vibration peak of GO is located at 1,628 cm^{-1}. The characteristic peaks at 1,155; 1,081; 1,030 and 947 cm^{-1} correspond to the C–O stretching vibration, O–H bending vibration, antisymmetric glycosidic C–O–C bond vibration and α-1,4-glycosidic bond skeleton vibration of β-CD, respectively [21,28,29]. Meanwhile, three absorption peaks appearing at 2,973; 2,928 and 876 cm^{-1} are attributable to the $–CH_3$ and $–CH_2$ vibration and Si–O bond symmetrical stretching of 3-MPTS, further evidencing the successful synthesis of β-CD/Fe_3O_4/GO-SH. In Fig. 3b, besides the above mentioned characteristic peaks, three new strong absorption peaks are emerging at 1,601; 1,384 and 1334 cm^{-1} representing the stretching vibrations of the aromatic ring, bending vibrations of methyl and methylene, from MB, respectively [30,31], verifying the successful adsorption of MB onto β-CD/Fe_3O_4/GO-SH.

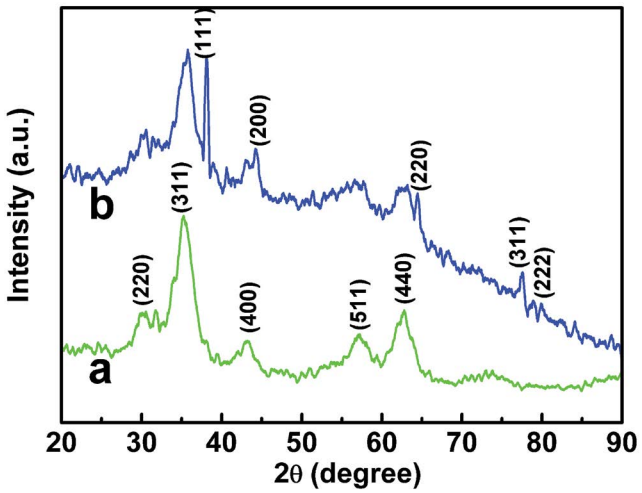

Fig. 2. XRD patterns of β-CD/Fe_3O_4/GO-SH before (a) and after (b) adsorption Ag(I).

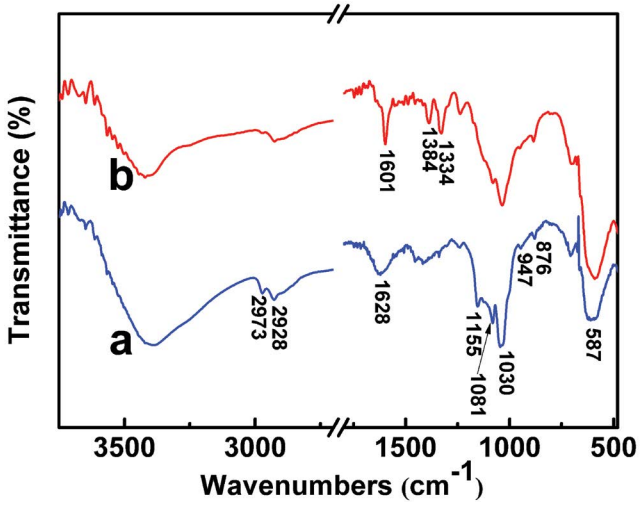

Fig. 3. FTIR spectra of β-CD/Fe_3O_4/GO-SH before (a) and after adsorption MB (b).

TGA was implemented to evaluate the thermal stability of β-CD/Fe_3O_4/GO-SH and the TGA curve is shown in Fig. 4. During the heating phase ranging from 25°C until 800°C at a heating rate of 10°C/min^{-1}, the weight loss processes of the β-CD/Fe_3O_4/GO-SH underwent three stages. The slight mass loss of β-CD/Fe_3O_4/GO-SH from the evaporation of the bound water occurs in the first step ranging from 61°C to 206°C. Up to 25.5% weight loss of β-CD/Fe_3O_4/GO-SH, appearing in the second stage between 206°C and 501°C is mainly attributed to the degradation of β-CD and thermal decomposition of oxygen-containing functional groups [32]. The 17.2% weight loss corresponds mainly to the cracking of the carbon skeleton, located in the final stage from 501°C to 800°C, with a total mass loss of 52.9% slightly lower than that of β-CD/Fe_3O_4/GO in our previous report [23], suggesting that the 3-MPTS modification improves the thermal stability of β-CD/Fe_3O_4/GO-SH.

The magnetic properties of β-CD/Fe_3O_4/GO-SH were determined using VSM at room temperature. From Fig. 5a, it could be noted that the magnetic hysteresis loop of β-CD/Fe_3O_4/GO-SH exhibits an S-type curve with negligible coercivity and remanence, implying that β-CD/Fe_3O_4/GO-SH possesses superparamagnetic. A saturation magnetization strength of β-CD/Fe_3O_4/GO-SH is 5.92 emu g^{-1}. As shown in the insets, β-CD/Fe_3O_4/GO-SH could be uniformly dispersed in the aqueous solution (Fig. 5b), and completely isolated under the presence of applied magnetic field (Fig. 5c), indicating that the magnetic properties of β-CD/Fe_3O_4/GO-SH completely meet the requirements of the solid–liquid phase magnetic separation.

As presented in Fig. 6, the N_2 adsorption/desorption isotherm (Fig. 6a) and BJH pore size distribution plots (Fig. 6b) were implemented to explore the textural properties of β-CD/Fe_3O_4/GO-SH. The isotherms of β-CD/Fe_3O_4/GO-SH are a type IV with type H3 hysteresis loop in conformity with IUPAC classification [33], reflecting the presence of mesopores in β-CD/Fe_3O_4/GO-SH and the irregular pore structure with cracks and wedges [34]. These cracks and wedges might generate from the gaps between Fe_3O_4 nanoparticles and the GO sheets themselves or each other. The average pore size is 7.49 nm calculated by BJH

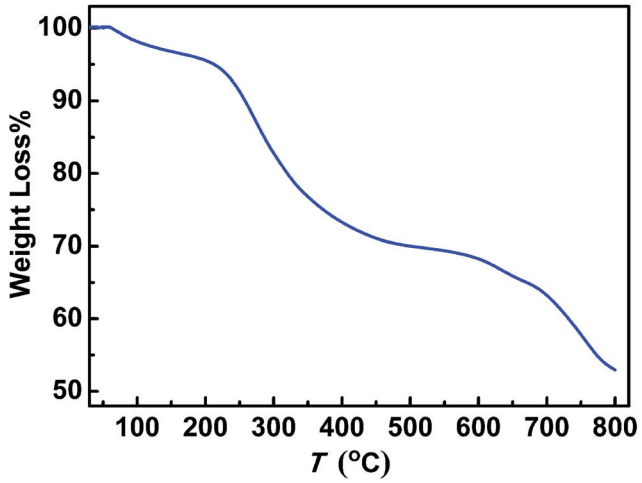

Fig. 4. TGA curve of β-CD/Fe_3O_4/GO-SH.

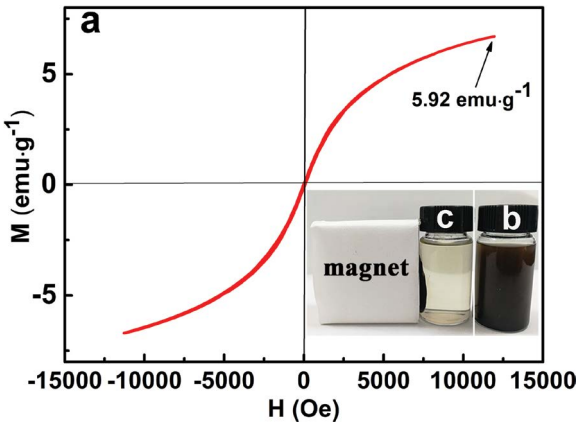

Fig. 5. Magnetic hysteresis loops for β-CD/Fe_3O_4/GO-SH (a), the insets of a digital photo of β-CD/Fe_3O_4/GO-SH dispersed in aqueous solution (b) and under an applied magnetic field (c).

theory. Simultaneously, these copious gaps endow β-CD/Fe_3O_4/GO-SH with a specific surface area of 76.56 m^2 g^{-1} and a cumulative pore volume of 0.19 cm^3 g^{-1}. Evidence for the mesoporous properties of β-CD/Fe_3O_4/GO-SH is further reinforced by the observation that most of the pores are distributed in size between 5 and 30 nm. As such, the structural characteristics of the β-CD/Fe_3O_4/GO-SH will facilitate the availability of adsorption sites and access to pollutants, thereby maximizing the removal efficiency.

XPS analysis was employed to identify the elemental compositions and the chemical valence of the β-CD/Fe_3O_4/GO-SH before and after adsorption Ag(I). From Fig. 7a, the peaks for C 1s, O 1s, S 2p, and Fe 2p are observed in the full survey XPS spectra before Ag(I) adsorption, indicating the presence of C, O, S and Fe elements in β-CD/Fe_3O_4/GO-SH and proof of the successful synthesis of β-CD/Fe_3O_4/GO-SH. In addition, the emergence of the well-defined characteristic peaks regarding Ag 3d, in the full survey XPS spectra after Ag(I) adsorption, demonstrates that Ag(I) was successfully adsorbed by β-CD/Fe_3O_4/GO-SH. Meanwhile, for the detection of the chemical valence of Ag(I) adsorbed on β-CD/Fe_3O_4/GO-SH, Fig. 7b shows the XPS high-resolution spectra of Ag 3d, where the appearance of energy peaks originating from Ag $3d_{3/2}$ and Ag $3d_{5/2}$ at 374.1 and 368.1 eV, respectively, indicates the reduction of Ag(I) to Ag element. The reason for the above results may be the coexistence of electron-rich functional groups such as –SH, –COOH, and –OH in β-CD/Fe_3O_4/GO-SH with strongly oxidizing Ag(I), resulting in the reduction of Ag(I) to metallic Ag, and revealing that the adsorption of Ag(I) could be carried out the redox reaction of –SH, –COOH and –OH with Ag(I) to form a complex [35]. The binding energies of the peaks corresponding to C–C, C–O, and C=O in the high-resolution spectra of C 1s before Ag(I) adsorption (Fig. 7c), remain at 284.8, 286.3 and 287.7 eV, respectively, after adsorption of Ag(I) (Fig. 7d) in exception to the altered peak intensity, pointing to the likelihood that the C atoms in the samples could not contribute to the adsorption of Ag(I). Alongside, the two energy peaks, corresponding to C=O and C–O at 532.3 and 531.6 eV in the high-resolution spectrum of O 1s before the Ag(I) adsorption (Fig. 7e), respectively shifted to the higher binding energy at 532.8 and 532.1 eV after the Ag(I) adsorption (Fig. 7f), and their intensity of the peaks noticeably become lower, which implies that O elements from carboxyl and hydroxyl functional groups interacted with Ag(I) during the process of the adsorption [36]. The high-resolution spectra of S 2p before Ag(I) adsorption (Fig. 7g) shows the characteristic peaks for S $2p_{3/2}$, S $2p_{1/2}$, and –C–S, which are located at the binding energies of 163.5, 164.6 and 168.9 eV, respectively. As exhibited in Fig. 7h, a significant alteration, related to both the position and intensity of the energy peaks regarding S 2p after Ag(I) adsorption, indicates the complexation of the S atoms [37] from the sulfhydryl functional groups in the β-CD/Fe_3O_4/GO-SH, and thus the presence of sulfhydryl groups exerts a critical influence on the adsorption of Ag(I). Summarized above, the predominant adsorption mechanism of β-CD/Fe_3O_4/GO-SH towards Ag(I) is the complexation of –COOH, –OH, and –SH with Ag(I).

3.2. Adsorption properties study

3.2.1. Effect of solution pH

The solution pH influences the ionization degree and molecular structure of the adsorbents to some extent, thus further affecting the adsorption efficiency. The effects of

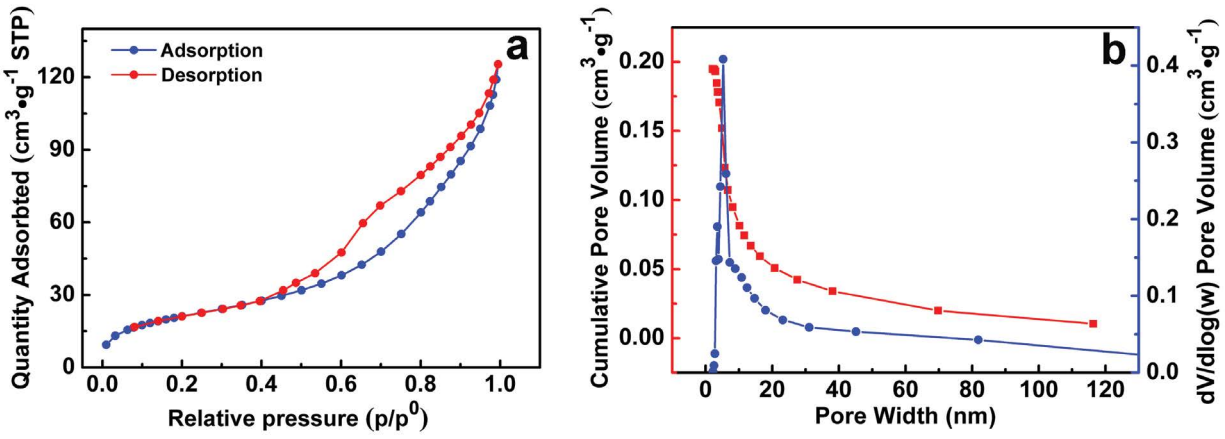

Fig. 6. N_2 adsorption/desorption isotherms (a) and BJH pore size distribution plots (b) of β-CD/Fe_3O_4/GO-SH.

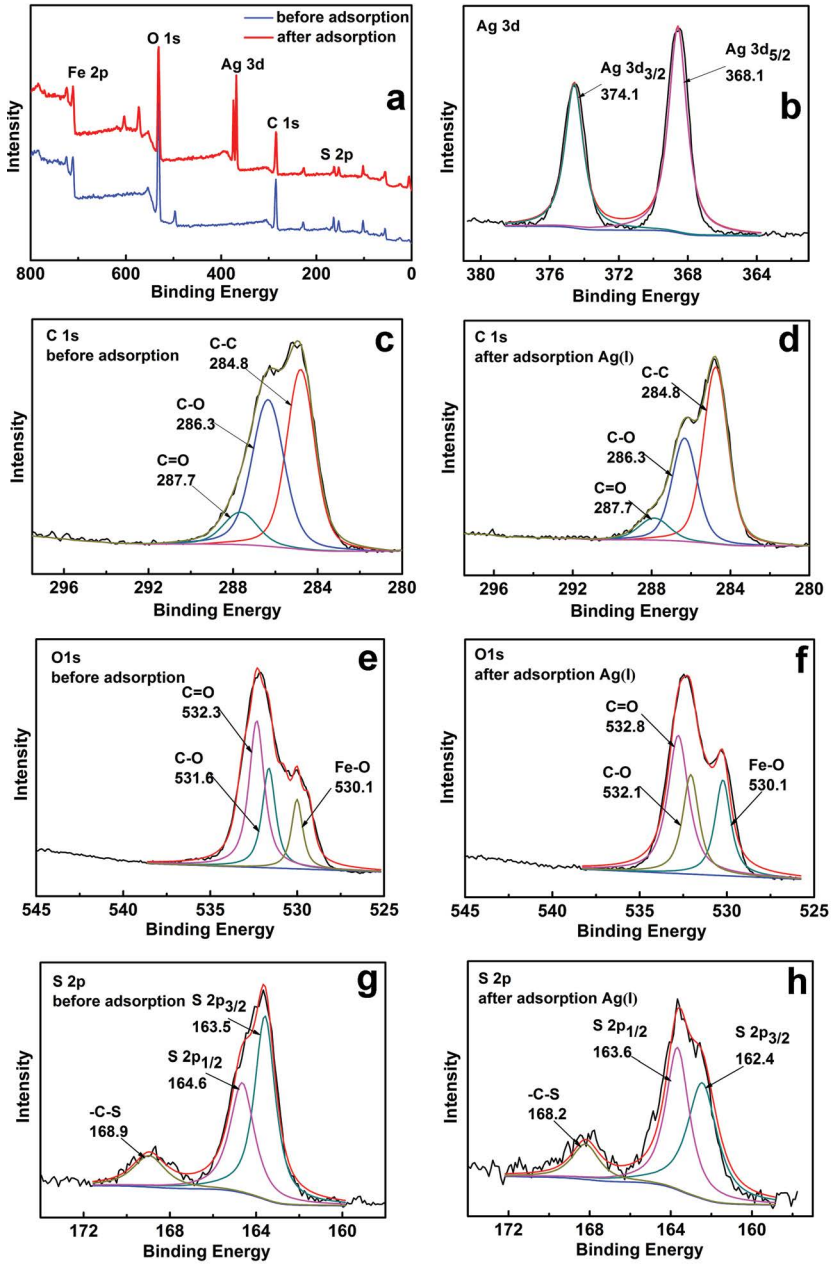

Fig. 7. The survey XPS spectra of β-CD/Fe_3O_4/GO-SH before and after adsorption Ag(I) (a), and corresponding high-resolution XPS spectra of Ag 3d (b), C 1s (c and d), O 1s (e and f) and S 2p (g and h).

solution pH on the adsorption capacity of β-CD/Fe_3O_4/GO-SH for Ag(I) and MB are represented in Fig. 8a. As observed in Fig. 8a, the adsorption capacity of β-CD/Fe_3O_4/GO-SH for the Ag(I) increases rapidly with the solution pH values increasing from 1.0 to 4.0. The increasing trend of adsorption capacity in pH value from 4.0 to 5.0 abruptly slows down, and the adsorption reaches equilibrium after a pH value of 5.0. For MB adsorption, the increasing trend in adsorption capacity is slow with the solution pH value increasing from 1.0 to 2.0, while a further increase at pH value of 4.0 is accompanied by a sharp ascent of the adsorption capacity and then a gradual approach to adsorption equilibrium at pH value of 5.0. The above phenomenon could be explained by considering the zeta potential of β-CD/Fe_3O_4/GO-SH in multiple pH values according to Fig. 8b. The adsorption sites of β-CD/Fe_3O_4/GO-SH were protonated at the solution pH value below the isoelectric point (pH_{zpc} = 4.5). As a result, the accumulation of positive charge on the β-CD/Fe_3O_4/GO-SH surface induced a ubiquitous electrostatic repulsion between Ag(I) or MB and the adsorbents, thus reducing the adsorption capacity of β-CD/Fe_3O_4/GO-SH for Ag(I) or MB. In conjunction with this, the high concentration of H^+ existing in low pH solutions could compete with Ag(I) or MB for binding sites on the adsorbent surface, thereby leading to a decline in adsorption capacity. With further increase of solution pH

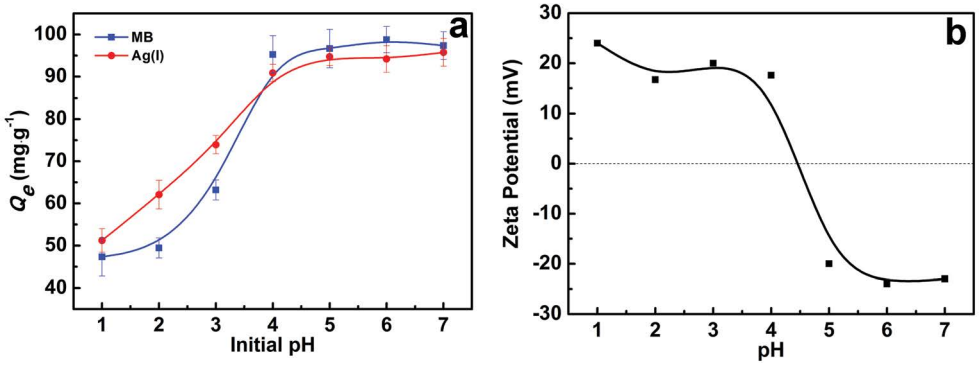

Fig. 8. Effect of solution pH on the adsorption of β-CD/Fe_3O_4/GO-SH for Ag(I) and MB (a) and zeta potential (b) of β-CD/Fe_3O_4/GO-SH. ($C_{0Ag(I)}$ = 150 mg L^{-1}; C_{0MB} = 200 mg L^{-1}; $t_{Ag(I)}$ = 10 h; t_{MB} = 2 h; T = 298 K).

value, the adsorption sites of β-CD/Fe_3O_4/GO-SH were deprotonated, and the negatively charged surface of the β-CD/Fe_3O_4/GO-SH was prone to attract positively charged Ag(I) or MB by electrostatic forces, followed by a stepwise increase of adsorption capacity.

3.2.2. Adsorption kinetic

The effect of contact time on Ag(I) (a) and MB (b) adsorption by β-CD/Fe_3O_4/GO-SH is shown in Fig. 9. The results from Fig. 9a show that the adsorption process of Ag(I) onto β-CD/Fe_3O_4/GO-SH underwent three stages during the whole period. The adsorption capacity of Ag(I) by β-CD/Fe_3O_4/GO-SH rises promptly with the contact time increasing within 15–60 min, the subsequent upward trend of adsorption capacity gradually retards with the extension of the contact time (60–240 min), until adsorption equilibrium is reached after 240 min. From Fig. 9b, the evolution process of β-CD/Fe_3O_4/GO-SH for MB adsorption nearly resembles that of Ag(I) adsorption.

From the above analysis, the adsorption process of β-CD/Fe_3O_4/GO-SH on Ag(I) and MB went through three stages of rapid adsorption, moderate adsorption, and equilibrium adsorption, which may be explained by the following reasons. At the initial phase, the adsorption rate is relatively quick on account of the existence of the heavy driving force derived from more active sites on the adsorbent surface and the high concentration of Ag(I) or MB. However, with the prolongation of contact time, the active sites on the adsorbent surface are occupied continuously, thereby Ag(I) or MB commences to diffuse into the interior of the adsorbent and the diffusion resistance became higher, which decelerates the adsorption rate. Later, the adsorption equilibrium is reached when the active sites, both interior and exterior of the adsorbent, are occupied by Ag(I) or MB.

To further determine rate-controlling steps of the adsorption process in terms of adsorption mechanism, the pseudo-first-order kinetic model, the pseudo-second-order kinetic model and the intraparticle diffusion model were employed to fit the kinetic experimental data, respectively, and the formal equations of the corresponding models are expressed in the following Eqs. (1)–(3), respectively [38–40].

$$\log\left(Q_e - Q_t\right) = \log Q_{e,\text{cal}} - \frac{k_1 t}{2.303} \tag{1}$$

$$\frac{t}{Q_t} = \frac{1}{k_2 Q_{e,\text{cal}}^2} + \frac{t}{Q_{e,\text{cal}}} \tag{2}$$

$$Q_t = k_i t^{1/2} + C \tag{3}$$

where k_1 (min^{-1}) and k_2 (g mg^{-1} min^{-1}), obtained from the slopes of linear plots, represent the equilibrium rate

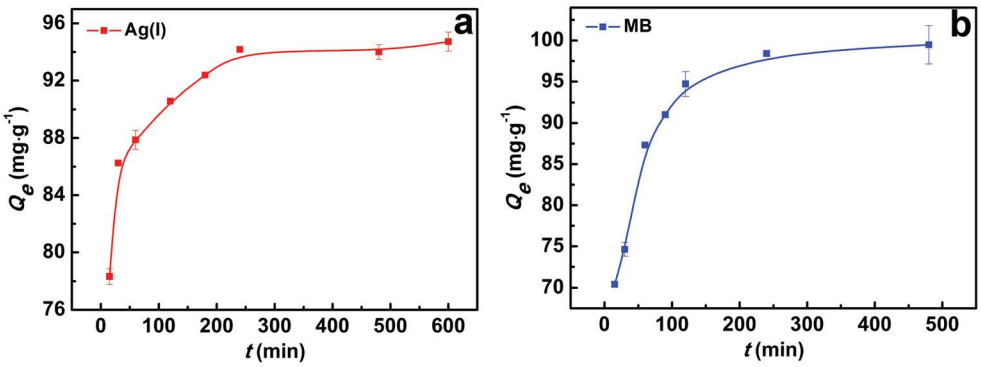

Fig. 9. Effect of contact time on the adsorption of β-CD/Fe_3O_4/GO-SH for Ag(I) (a) and MB (b). ($C_{0Ag(I)}$ = 150 mg L^{-1}; C_{0MB} = 200 mg L^{-1}; $pH_{Ag(I)}$ = 5.8; pH_{MB} = 5.4; T = 298 K).

constants of the pseudo-first-order kinetic model and the pseudo-second-order kinetic model, as well as Q_e (mg g^{-1}) and Q_t (mg g^{-1}) are the adsorption capacity at the time of adsorption equilibrium and contact time t, respectively. $Q_{e,cal}$ (mg g^{-1}) is equilibrium adsorption capacity calculated from kinetic models formal equation. k_i (mg g^{-1} min$^{-1/2}$) stands for the intraparticle diffusion rate constant, and C (mg g^{-1}) is a constant for thickness of boundary layer.

The linear plots of the pseudo-first-order kinetic model (a) and pseudo-second-order kinetic model (b) for Ag(I) and MB adsorption on β-CD/Fe_3O_4/GO-SH are depicted in Fig. 10, respectively. As apparently discernible from the fitted linear plots, the correlation coefficient of the pseudo-second-order kinetic model is closer to 1 in comparison to that of the pseudo-first-order kinetic model. The above analytical conclusions forcefully attest to the suitability of the pseudo-second-order kinetic model for the description of the adsorbed process. Accordingly, the primary adsorption mechanisms of β-CD/Fe_3O_4/GO-SH for Ag(I) and MB are chemisorption based on host-guest complexation, electrostatic interactions, and π–π conjugation [41,42], where for Ag(I), the adsorption mechanism also involves complexation, as evidenced by the results of XPS analysis.

The intraparticle diffusion model offered by Weber and Morris is adopted to evaluate the experimental data to define the rate-limiting step during the adsorption process. Fig. 11 presents the results of the intraparticle diffusion model for Ag(I) and MB adsorption onto β-CD/Fe_3O_4/GO-SH, as shown that the multilinear plots for Q_t vs. $t^{1/2}$ are partitioned into three segments. And from Table 1, the order of the diffusion rate constants in each segment of the plots are as follows: $k_{i1} > k_{i2} > k_{i3}$, which confirms that the first linear segment is the rapid adsorption step, representing the collision of Ag(I) or MB with each other in the bulk solution, and the speedy movement to the adsorbent surface and binding to the active sites. The second linear portion is attributed to the decline in the adsorption rate as a result of the diffusion of Ag(I) or MB into the internal pores. The slope of the final fraction reaching a minimum reflects the adsorption equilibrium step, explained by the lower concentration of adsorbate and the amounts of available active sites [43]. Moreover, none of the linear segments passes through the origin (the C value is non-zero), signifying that intraparticle diffusion is not the only rate-controlling step in the overall adsorption process [44].

3.2.3. Adsorption isotherms

The effect of the initial concentration of Ag(I) (a) and MB (b) solutions on the adsorption performance of β-CD/Fe_3O_4/GO-SH is depicted in Fig. 12, it is observed that the

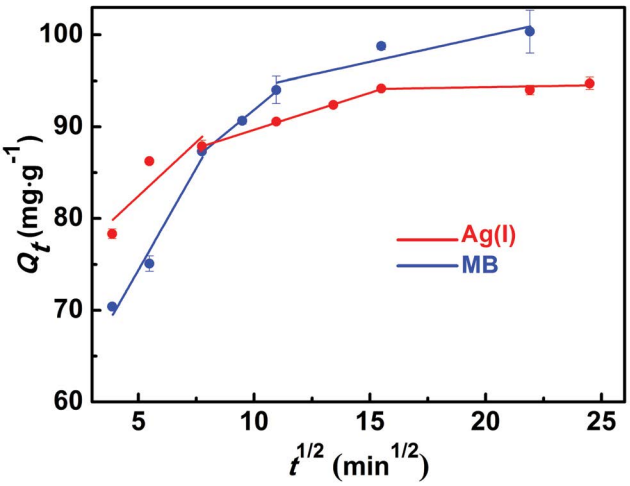

Fig. 11. Intraparticle diffusion models of Ag(I) and MB adsorption onto β-CD/Fe_3O_4/GO-SH.

Table 1
Parameters of intraparticle diffusion model for Ag(I) and MB adsorption onto β-CD/Fe_3O_4/GO-SH

Target	Constants (mg g^{-1} min$^{-1/2}$)		R^2	C_i (mg g^{-1})
Ag(I)	k_{i1}	2.3509	0.6010	70.75
	k_{i2}	0.8070	0.9987	81.65
	k_{i3}	0.0433	0.9863	93.41
MB	k_{i1}	4.4344	0.9539	52.33
	k_{i2}	2.0816	0.9952	71.10
	k_{i3}	0.5570	0.7252	88.73

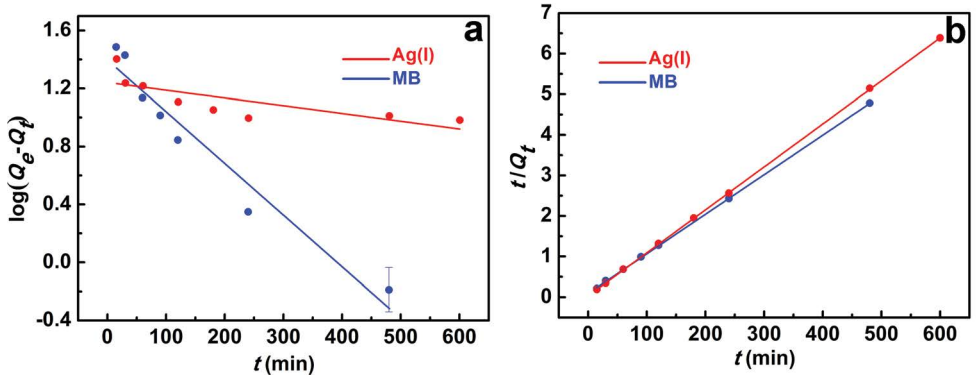

Fig. 10. The pseudo-first-order kinetic (a) and pseudo-second-order kinetic models (b) for the adsorption of Ag(I) and MB on β-CD/Fe_3O_4/GO-SH.

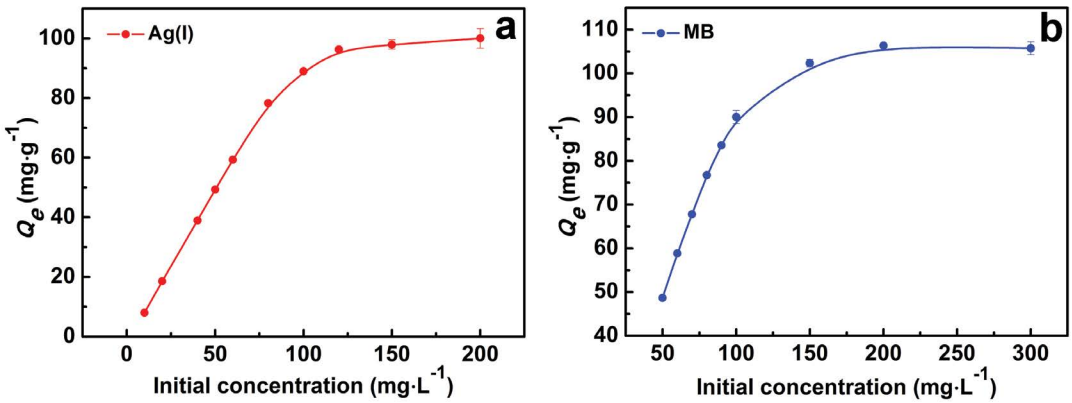

Fig. 12. Effect of initial concentration on the adsorption of β-CD/Fe_3O_4/GO-SH for Ag(I) (a) and MB (b). ($t_{Ag(I)}$ = 10 h; t_{MB} = 2 h; $pH_{Ag(I)}$ = 5.8; pH_{MB} = 5.4; T = 298 K).

adsorption capacity increases with the initial concentration and eventually plateaus, which is attributed to the fact that with the increase of the solution concentration, the mass transfer driving force generated by the abundant unoccupied active sites and high concentration difference promoting the rapid diffusion of the adsorbate to the adsorbent surface and binding with the active sites. With the initial concentration continuing to increase, the adsorption equilibrium was attained after more active adsorbent sites were occupied. The maximum adsorption capacities of β-CD/Fe_3O_4/GO-SH for Ag(I) and MB are 101.87 and 105.74 mg g^{-1}, respectively. From Table 2, it can be surmised that β-CD/Fe_3O_4/GO-SH is an effective adsorbent for adsorption of Ag(I) and MB in aqueous solution compared to other reported adsorbents.

The adsorption isotherm model is an indispensable reference for explanations of the adsorption mechanism, which could mirror the interaction behavior between the adsorbate and the adsorbent. Hence, four well-known isothermal models, the Langmuir, Freundlich, Temkin, and Dubinin–Radushkevich (D-R) isotherms models [53] are utilized to describe the equilibrium isotherm of the adsorption process.

The Langmuir isothermal model assumes the uptake of adsorbate through monolayer adsorption on a homogeneous surface and no interaction between the adsorbed molecules. The linear mathematical Eq. (4) of the Langmuir model is expressed as follows.

$$\frac{C_e}{Q_e} = \frac{1}{K_L Q_m} + \frac{C_e}{Q_m} \tag{4}$$

where Q_m (mg g^{-1}) denotes the maximum adsorption capacity of β-CD/Fe_3O_4/GO-SH for adsorbate. Q_e (mg g^{-1}) and C_e (mg L^{-1}) respectively represent the adsorption equilibrium capacity and the corresponding adsorbate concentration. K_L (L mg^{-1}) stands for the Langmuir equilibrium constant associated with the affinity of binding sites.

According to the Freundlich isotherm model, there is non-uniform multilayer adsorption of adsorbate molecules on the heterogeneous surface of the adsorbent, which means that the affinity of the binding sites on the adsorbent surface varies with the interaction between the adsorbed molecules. The linear form of the Freundlich model is written as Eq. (5).

Table 2
Comparison of the maximum adsorption capacity of β-CD/Fe_3O_4/GO-SH and other adsorbents for Ag(I) and MB

Adsorbents	Maximum adsorption capacity (mg g^{-1})		Ref.
	Ag(I)	MB	
SSBs	75.8	–	[33]
SE-SNPs	21.9	–	[45]
(MNP-G3)	2.84	–	[46]
mGO@SiO_2@PPy-PTh.	49	–	[47]
AC/γ-Fe_2O_3-BPDM	32.6	–	[48]
Fe_3O_4@SiO_2@$SiC_3H_6NH_2$/poly(2-aminothiophenol)	52.3	–	[49]
NC-cotton	–	95.8	[50]
Gelatin/β-CD	–	47.4	[51]
PCL/PCD	–	10.5	[52]
β-CD/Fe_3O_4/GO-SH	101.87	105.74	This work

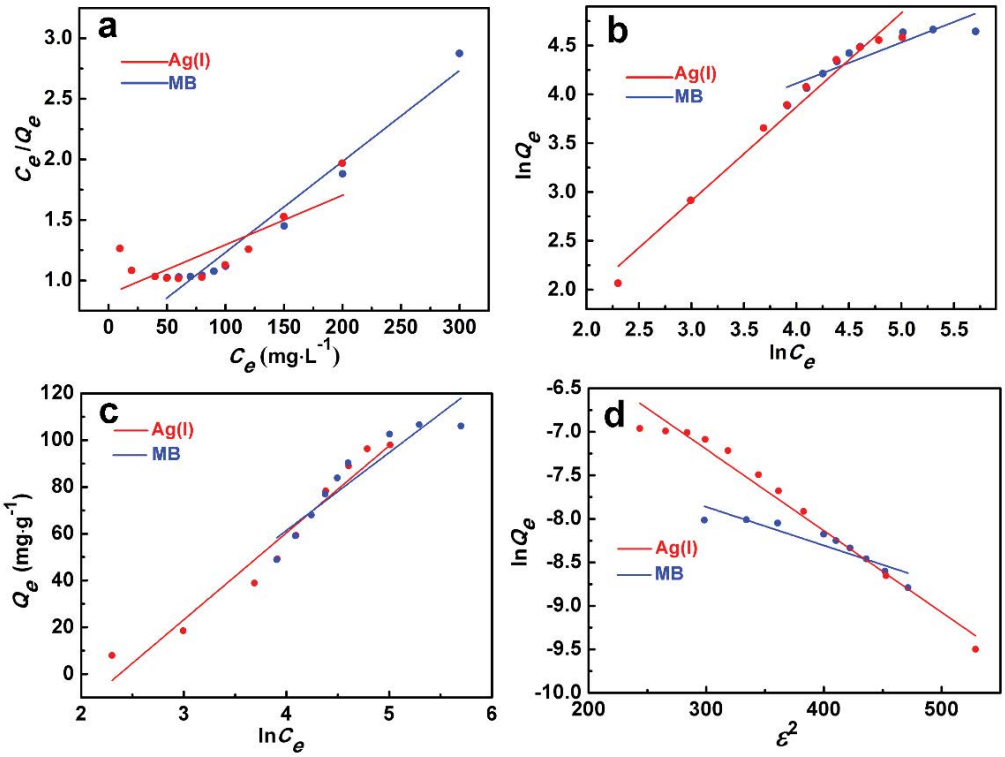

Fig. 13. Langmuir (a), Freundlich (b), Temkin (c), and Dubinin–Radushkevich (d) adsorption equilibrium isotherms for adsorption of Ag(I) and MB on β-CD/Fe_3O_4/GO-SH.

$$\ln Q_e = \ln K_F + \frac{1}{n}\ln C_e \tag{5}$$

where K_F (mg^{1-n} L^n g^{-1}) and n symbolize the Freundlich empirical constant governing adsorption capacity and adsorption intensity, respectively.

The Temkin isotherm model assumes a linear rather than logarithmic increase in the heat of adsorption as the adsorbate molecules cover the adsorbent surface, the mathematical expression as Eq. (6).

$$Q_e = \frac{RT}{b_T}\ln C_e + \frac{RT}{b_T}\ln K_T \tag{6}$$

where K_T is the equilibrium constant with respect to the maximum binding energy. R and T are gas constant (8.314 J mol^{-1} K^{-1}) absolute temperature (K), respectively, and hence RT/b_T is the empirical constant relevant to the heat of adsorption.

The D-R isotherm commonly postulates that the adsorption mechanism is compliant with a Gaussian energy distribution over a heterogeneous surface and is mathematically expressed in Eq. (7).

$$\ln Q_e = \ln Q_m - K_{\text{D-R}}\varepsilon^2 \tag{7}$$

where $K_{\text{D-R}}$ (mol^2 kJ^{-2}) is the isothermal constant and also signifies the activity coefficient correlated with the average adsorption energy. Q_m and Q_e (mol g^{-1}) is the highest value of the adsorption capacity of the adsorbent on the adsorbate molecules and the amount of adsorption at equilibrium, respectively. The Polanyi sorption potential (ε) is calculated by Eq. (8).

$$\varepsilon = RT\ln\left(1+\frac{1}{C_e}\right) \tag{8}$$

where C_e (mol L^{-1}) represents the adsorbate equilibrium concentration. E (kJ mol^{-1}) means Gibbs free energy of per absorbing molecule during transport from infinity to solution, is obtained from Eq. (9).

$$E = \frac{1}{\sqrt{2K_{\text{D-R}}}} \tag{9}$$

The value of E less than 8 kJ mol^{-1}, the adsorption process is dominated by physisorption, if the value of E is between 8 and 16 kJ mol^{-1}, chemisorption is primary.

Fig. 13 shows the adsorption equilibrium isotherms obtained from fitting the experimental data of β-CD/Fe_3O_4/GO-SH adsorption for Ag(I) and MB by the Langmuir (a), Freundlich (b), Temkin (c), and D-R isotherm models (d), respectively. For Ag(I) adsorption, the correlation coefficient of the Freundlich model is closer to 1 than that of other models. That is the establishment of multilayer adsorption of Ag(I) on the adsorbent surface, confirming the existence of active sites with diverse affinities for Ag(I) on the β-CD/Fe_3O_4/GO-SH surface, which is possibly ascribed

to greater affinity of the sulfhydryl functional groups for Ag(I) than other active sites on the β-CD/Fe_3O_4/GO-SH surface, such as hydroxyl and carboxyl groups [54]. Moreover, the excellent effectiveness of β-CD/Fe_3O_4/GO-SH for Ag(I) adsorption is revealed by the constant $1/n$ ($0.5 < 1/n < 1$) correlated with the adsorption intensity [41]. For MB adsorption, the correlation coefficient of the Langmuir model is closer to 1 than that of other models. The results predict homogeneous monolayer adsorption of MB on the β-CD/Fe_3O_4/GO-SH surface. Further, the adsorption energies (E) of the adsorbents for MB and Ag(I) are 10.23 and 8.19 kJ mol^{-1}, respectively, implying that the adsorption process was predominant chemisorption.

3.3. Cost-estimation

The cost of the adsorbent lies mainly in the raw material and the synthesis method. β-CD is a low-cost natural cyclic oligosaccharide derived from enzymatic hydrolysis of starch [17]. Fe_3O_4 nanoparticles were synthesized using low-cost $FeCl_3{\cdot}6H_2O$ and $FeSO_4{\cdot}7H_2O$ as precursors. And we used the extremely inexpensive natural flake graphite as the raw material for the synthesis of GO, further reducing its preparation cost. Besides, the method for the preparation of this adsorbent is simple, eco-friendly, low energy expenditure, eliminating many tedious synthesis procedures, thus reducing unnecessary costs to some extent. Hence, the β-CD/Fe_3O_4/GO-SH has promise as an efficient adsorbent for the removal of MB and Ag(I) from aqueous solutions.

4. Conclusions

- The β-CD/Fe_3O_4/GO-SH was successfully fabricated and exhibited superparamagnetic properties and the saturation magnetization strength met the requirements of magnetic separation.
- The sulfhydryl functional group on β-CD/Fe_3O_4/GO-SH exerted a superior affinity for Ag(I), and Ag(I) was reduced to Ag element during the adsorption process.
- The maximum adsorption capacity of β-CD/Fe_3O_4/GO-SH for Ag(I) and MB was 101.87 and 105.74 mg g^{-1}, respectively.
- The adsorption kinetics and isotherms studies showed that the adsorption processes of β-CD/Fe_3O_4/GO-SH for Ag(I) and MB involved predominantly chemisorption in heterogeneous multilayer and homogeneous monolayer, respectively.

Acknowledgments

The authors are grateful for financial support from the National Natural Science Foundation of China (No. 51403091, 51663013) and the Joint Fund between Shenyang National Laboratory for Materials Science and State Key Laboratory of Advanced Processing and Recycling of Nonferrous Metals (No. 18LHPY005).

References

[1] M.J. Eckelman, T.E. Graedel, Silver emissions and their environmental impacts: a multilevel assessment, Environ. Sci. Technol., 41 (2007) 6283–6289.
[2] Z.Y. Chen, P. Yang, Z.G. Yuan, J.H. Guo, Aerobic condition enhances bacteriostatic effects of silver nanoparticles in aquatic environment: an antimicrobial study on *Pseudomonas aeruginosa*, Sci. Rep., 7 (2017) 7398–7405.
[3] Y.B. Zhou, J. Lu, Y. Zhou, Y.D. Liu, Recent advances for dyes removal using novel adsorbents: a review, Environ. Pollut., 252 (2019) 352–365.
[4] S. Soni, P.K. Bajpai, J. Mittal, C. Arora, Utilisation of cobalt doped Iron based MOF for enhanced removal and recovery of methylene blue dye from waste water, J. Mol. Liq., 314 (2020) 113642–113653.
[5] J. Mittal, Permissible synthetic food dyes in India, Resonance-J. Sci. Educ., 25 (2020) 567–577.
[6] I. Anastopoulos, A. Mittal, M. Usman, J. Mittal, G.H. Yu, A. Núñez-Delgado, M. Kornaros, A review on halloysite-based adsorbents to remove pollutants in water and wastewater, J. Mol. Liq., 269 (2018) 855–868.
[7] V.K. Gupta, S. Agarwal, R. Ahmad, A. Mirza, J. Mittal, Sequestration of toxic congo red dye from aqueous solution using ecofriendly guar gum/activated carbon nanocomposite, Int. J. Biol. Macromol., 158 (2020) 1310–1318.
[8] H. Daraei, A. Mittal, Investigation of adsorption performance of activated carbon prepared from waste tire for the removal of methylene blue dye from wastewater, Desal. Water Treat., 90 (2017) 294–298.
[9] A. Mittal, J. Mittal, A. Malviya, V.K. Gupta, Removal and recovery of Chrysoidine Y from aqueous solutions by waste materials, J. Colloid Interface Sci., 344 (2010) 497–507.
[10] C. Arora, S. Soni, S. Sahu, J. Mittal, P. Kumar, P.K. Bajpai, Iron based metal organic framework for efficient removal of methylene blue dye from industrial waste, J. Mol. Liq., 284 (2019) 343–352.
[11] C. Arora, D. Sahu, D. Bharti, V. Tamrakar, S. Soni, S. Sharma, Adsorption of hazardous dye crystal violet from industrial waste using low-cost adsorbent *Chenopodium album*, Desal. Water Treat., 167 (2019) 324–332.
[12] X. Qin, L. Bai, Y. Tan, L. Li, F. Song, Y.Z. Wang, β-Cyclodextrin-crosslinked polymeric adsorbent for simultaneous removal and stepwise recovery of organic dyes and heavy metal ions: fabrication, performance and mechanisms, Chem. Eng. J., 372 (2019) 1007–1018.
[13] J.-H. Xue, H. Zhang, D.X. Ding, N. Hu, Y.-D. Wang, Y.-S. Wang, Linear β-cyclodextrin polymer functionalized multiwalled carbon nanotubes as nanoadsorbent for highly effective removal of U(VI) from aqueous solution based on inner-sphere surface complexation, ACS Ind. Eng. Chem. Res., 58 (2019) 4074–4083.
[14] P. Xu, G.M. Zeng, D.L. Huang, C.L. Feng, S. Hu, M.H. Zhao, C. Lai, Z. Wei, C. Huang, G.X. Xie, Z.F. Liu, Use of iron oxide nanomaterials in wastewater treatment: a review, Sci. Total Environ., 424 (2012) 1–10.
[15] G. Sheng, Y. Li, X. Yang, X.M. Ren, S.T. Yang, J. Hu, X.K. Wang, Efficient removal of arsenate by versatile magnetic graphene oxide composites, RSC Adv., 2 (2012) 12400–12407.
[16] M.V. Rekharsky, Y. Inoue, Complexation thermodynamics of cyclodextrins, Chem. Rev., 98 (1998) 1875–1917.
[17] Z. Wang, F. Cui, Y. Pan, L.X. Hou, B. Zhang, Y.Q. Li, L.P. Zhu, Hierarchically micro-mesoporous beta-cyclodextrin polymers used for ultrafast removal of micropollutants from water, Carbohydr. Polym., 213 (2019) 352–360.
[18] J.H. Chen, D.Q. Lu, B. Chen, P.K. OuYang, Removal of U(VI) from aqueous solutions by using MWCNTs and chitosan modified MWCNTs, J. Radioanal. Nucl. Chem., 295 (2012) 2233–2241.
[19] J. Li, S. Zhang, C. Chen, G.X. Zhao, X. Yang, J.K. Li, X.K. Wang, Removal of Cu(II) and fulvic acid by graphene oxide nanosheets decorated with Fe_3O_4 nanoparticles, ACS Appl. Mater. Interfaces, 4 (2012) 4991–5000.
[20] D. Wang, L. Liu, X. Jiang, J. Yu, X. Chen, Adsorption and removal of malachite green from aqueous solution using magnetic β-cyclodextrin-graphene oxide nanocomposites as adsorbents, Colloids Surf., A, 466 (2015) 166–173.
[21] H. Wang, Y.G. Liu, G.M. Zeng, X.J. Hu, X. Hu, T.T. Li, H.Y. Li, Y.Q. Wang, L.H. Jiang, Grafting of beta-cyclodextrin to magnetic

graphene oxide via ethylenediamine and application for Cr(VI) removal, Carbohydr. Polym., 113 (2014) 166–173.
[22] Y. Chen, S. Cao, L. Zhang, C. Xi, X. Li, Z. Chen, G. Wang, Preparation of size-controlled magnetite nanoparticles with a graphene and polymeric ionic liquid coating for the quick, easy, cheap, effective, rugged and safe extraction of preservatives from vegetables, J. Chromatogr. A, 1448 (2016) 9–19.
[23] Y.X. Ma, W.J. Shao, W. Sun, Y.L. Kou, X. Li, H.P. Yang, One-step fabrication of β-cyclodextrin modified magnetic graphene oxide nanohybrids for adsorption of Pb(II), Cu(II) and methylene blue in aqueous solutions, Appl. Surf. Sci., 459 (2018) 544–553.
[24] R. Randazzo, A.D. Mauro, A. D'Urso, G.C. Messina, G. Compagnini, V. Villari, N. Micali, R. Purrello, M.E. Fragala, Hierarchical effect behinds the supramolecular chirality of silver(I)-cysteine coordination polymers, ACS J. Phys. Chem. B, 119 (2015) 4898–4904.
[25] D.C. Marcano, D.V. Kosynkin, J.M. Berlin, A. Sinitskii, Z.Z. Sun, C. Slesarev, L.B. Alemany, W. Lu, J.M. Tour, Improved synthesis of graphene oxide, ACS Nano, 4 (2010) 4806–4814.
[26] L. Cui, Y. Wang, L. Gao, L. Hu, L. Yan, Q. Wei, B. Du, EDTA functionalized magnetic graphene oxide for removal of Pb(II), Hg(II) and Cu(II) in water treatment: adsorption mechanism and separation property, Chem. Eng. J., 281 (2015) 1–10.
[27] R. Ghosh, D. Ekka, B. Rajbanshi, A. Yasmina, M.N. Roya, Synthesis, characterization of 1-butyl-4-methylpyridinium lauryl sulfate and its inclusion phenomenon with β-cyclodextrin for enhanced applications, Colloids Surf., A, 548 (2018) 206–217.
[28] L. Lin, C. Zou, Kinetic and thermodynamic study of magnetic separable β-cyclodextrin inclusion complex with organic phosphoric acid applied to removal of Hg^{2+}, ACS J. Chem. Eng. Data, 62 (2017) 762–772.
[29] T. Guo, A.H. Bedane, Y. Pan, B. Shirani, H.N. Xiao, M. Eic, Adsorption characteristics of carbon dioxide gas on a solid acid derivative of β-cyclodextrin, ACS Energy Fuel, 31 (2017) 4186–4192.
[30] M. Munir, M.F. Naza, M.N. Zafar, M. Zubair, M. Ashfaq, A. Hosseini-Bandegharaei, S.U. Khan, A. Ahmad, Effective adsorptive removal of methylene blue from water by didodecyldimethylammonium bromide-modified brown clay, ACS Omega, 5 (2020) 16711–16721.
[31] R.M. Novais, J. Carvalheiras, D.M. Tobaldi, M.P. Seabra, R.C. Pullar, J.A. Labrincha, Synthesis of porous biomass fly ash-based geopolymer spheres for efficient removal of methylene blue from wastewaters, J. Cleaner Prod., 207 (2019) 350–362.
[32] R. Sedghi, B. Heidari, M. Yassari, Novel molecularly imprinted polymer based on beta-cyclodextrin@graphene oxide: synthesis and application for selective diphenylamine determination, J. Colloid Interface Sci., 503 (2017) 47–56.
[33] D.V. Quang, J.E. Lee, J.K. Kim, Y.N. Kim, G.N. Shao, H.K. Kim, A gentle method to graft thiol-functional groups onto silica gel for adsorption of silver ions and immobilization of silver nanoparticles, Powder Technol., 235 (2013) 221–227.
[34] M. Liu, B. Zhang, H. Wang, F. Zhao, Y. Chen, Q. Sun, Facile crosslinking synthesis of hyperbranch-substrate nanonetwork magnetite nanocomposite for the fast and highly efficient removal of lead ions and anionic dyes from aqueous solutions, RSC Adv., 6 (2016) 67057–67071.
[35] T. Mahlangu, R. Das, L.K. Abia, M. Onyango, S.S. Ray, A. Maity, Thiol-modified magnetic polypyrrole nanocomposite: an effective adsorbent for the adsorption of silver ions from aqueous solution and subsequent water disinfection by silver-laden nanocomposite, Chem. Eng. J., 360 (2019) 423–434.
[36] L.A. Romero-Cano, H. García-Rosero, M. del Olmo-Iruela, F. Carrasco-Marín, L.V. González-Gutiérrez, Use of carbon paste electrodes as a novel strategy to study adsorption mechanism of silver ions onto functionalized grapefruit peel, J. Electroanal. Chem., 830–831 (2018) 20–26.
[37] P. Liu, X. Wang, L. Tian, B. He, X. Lv, X. Li, C. Wang, L. Song, Adsorption of silver ion from the aqueous solution using a polyvinylidene fluoride functional membrane bearing thiourea groups, J. Water Process Eng., 34 (2020) 101184–101194.
[38] Y.S. Ho, G. McKay, Pseudo-second order model for sorption processes, Process Biochem., 34 (1999) 451–465.
[39] J. Febrianto, A.N. Kosasih, J. Sunarso, Y.H. Ju, N. Indraswati, S. Ismadji, Equilibrium and kinetic studies in adsorption of heavy metals using biosorbent: a summary of recent studies, J. Hazard. Mater., 162 (2009) 616–645.
[40] H. Tang, W. Zhou, L. Zhang, Adsorption isotherms and kinetics studies of malachite green on chitin hydrogels, J. Hazard. Mater., 209–210 (2012) 218–225.
[41] Z. Li, X. Huang, K. Wu, Y. Jiao, C. Zhou, Fabrication of regular macro-mesoporous reduced graphene aerogel beads with ultra-high mechanical property for efficient bilirubin adsorption, Mater. Sci. Eng. C., 106 (2020) 110282, doi: 10.1016/j.msec.2019.110282.
[42] S.H. Shaikh, S.A. Kumar, Polyhydroxamic acid functionalized sorbent for effective removal of chromium from ground water and chromic acid cleaning bath, Chem. Eng. J., 326 (2017) 318–328.
[43] N. Tang, C.G. Niu, X.T. Li, C. Liang, H. Guo, L.S. Lin, C.W. Zheng, G.M. Zeng, Efficient removal of Cd^{2+} and Pb^{2+} from aqueous solution with amino- and thiol-functionalized activated carbon: isotherm and kinetics modeling, Sci. Total Environ., 635 (2018) 1331–1344.
[44] W.H. Cheung, Y.S. Szeto, G. McKay, Intraparticle diffusion processes during acid dye adsorption onto chitosan, Bioresour. Technol., 98 (2007) 2897–2904.
[45] L. Zhang, G. Zhang, S. Wang, J.H. Peng, W. Cui, Sulfoethyl functionalized silica nanoparticle as an adsorbent to selectively adsorbe silver ions from aqueous solutions, J. Taiwan Inst. Chem. Eng., 71 (2017) 330–337.
[46] C.H. Yen, H.L. Lien, J.S. Chung, H.D. Yeh, Adsorption of precious metals in water by dendrimer modified magnetic nanoparticles, J. Hazard. Mater., 322 (2017) 215–222.
[47] N. Jalilian, H. Ebrahimzadeh, A.A. Asgharinezhad, K. Molaei, Extraction and determination of trace amounts of gold(III), palladium(II), platinum(II) and silver(I) with the aid of a magnetic nanosorbent made from Fe_3O_4-decorated and silica-coated graphene oxide modified with a polypyrrole-polythiophene copolymer, Microchim. Acta, 184 (2017) 2191–2200.
[48] M. Ghanei-Motlagh, M. Fayazi, M.A. Taher, A. Jalalinejad, Application of magnetic nanocomposite modified with a thiourea based ligand for the preconcentration and trace detection of silver ions(I) by electrothermal atomic absorption spectrometry, Chem. Eng. J., 290 (2016) 53–62.
[49] R, sedghi, M, Shojaee, M, Behbahani, M.Z. Nabid, Application of magnetic nanoparticles modified with poly (2-amino thiophenol) as a sorbent for solid phase extraction and trace detection of lead, copper and silver ions in food matrices, RSC Adv., 5 (2015) 67418–67426.
[50] X. Yue, F. Jiang, D. Zhang, H. Lin, Y. Chen, Preparation of adsorbent based on cotton fiber for removal of dyes, Fibers Polym., 18 (2017) 2102–2110.
[51] Y. Chen, Y. Ma, W. Lu, Y. Guo, Y. Zhu, H. Lu, Y. Song, Environmentally friendly gelatin/β-cyclodextrin composite fiber adsorbents for the efficient removal of dyes from wastewater, Molecules, 23 (2018) 2473–2489.
[52] R. Guo, R. Wang, J. Yin, T. Jiao, H. Huang, X. Zhao, L. Zhang, Q. Li, J. Zhou, Q. Peng, Fabrication and highly efficient dye removal characterization of beta-cyclodextrin-based composite polymer fibers by electrospinning, Nanomaterials, 9 (2019) 127–143.
[53] V. Kumar, P. Saharan, A.K. Sharma, A. Umar, I. Kaushal, A. Mittal, Y. Al-Hadeethi, B. Rashad, Silver doped manganese oxide-carbon nanotube nanocomposite for enhanced dye-sequestration: Isotherm studies and RSM modelling approach, Ceram. Int., 46 (2020) 10309–10319.
[54] Q.S. Huang, W. Wu, W. Wei, B.J. Ni, Polyethylenimine modified potassium tungsten oxide adsorbent for highly efficient Ag^+ removal and valuable Ag^0 recovery, Sci. Total Environ., 692 (2019) 1048–1056.